

Type-Ia Supernova-driven Galactic Bulge Wind

Shikui Tang¹, Q. Daniel Wang¹, Mordecai-Mark Mac Low^{2,3}, and M. Ryan Joung⁴

¹*Department of Astronomy, University of Massachusetts, Amherst, MA 01003*

²*Dept. of Astrophysics, American Museum of Natural History*

³*Dept. of Astronomy, Columbia University*

⁴*Dept. of Astrophysical Sciences, Princeton University*

ABSTRACT

Stellar feedback in galactic bulges plays an essential role in shaping the evolution of galaxies. To quantify this role and facilitate comparisons with X-ray observations, we conduct three-dimensional (3D) hydrodynamical simulations with the adaptive mesh refinement code, FLASH, to investigate the physical properties of hot gas inside a galactic bulge, similar to that of our Galaxy or M31. We assume that the dynamical and thermal properties of the hot gas are dominated by mechanical energy input from supernovae (SNe), primarily Type Ia, and mass injection from evolved stars as well as iron enrichment from SNe. We study the bulge-wide outflow as well as the SN heating on scales down to ~ 4 pc. An embedding scheme that is devised to plant individual SN remnant (SNR) seeds, allows to examine, for the first time, the effect of sporadic SNe on the density, temperature, and iron ejecta distribution of the hot gas as well as the resultant X-ray morphology and spectrum. We find that the SNe produce a bulge wind with highly filamentary density structures and patchy ejecta. Compared with a one-dimensional (1D) spherical wind model, the non-uniformity of simulated gas density, temperature, and metallicity substantially alters the spectral shape and increases the diffuse X-ray luminosity. The differential emission measure as a function of temperature of the simulated gas exhibits a log-normal distribution, with a peak value much lower than that of the corresponding 1D model. The X-ray luminosity depends sensitively on the mass loss rate from evolved stars. The bulk of the X-ray emission comes from the relatively low temperature and low abundance gas shells associated with SN blastwaves. SN ejecta are not well mixed with the ambient medium, at least in the bulge region. These results, at least partly, account for the apparent lack of evidence for iron enrichment in the soft X-ray-emitting gas in galactic bulges and intermediate-mass elliptical galaxies. The bulge wind helps to explain the “missing” stellar feedback in such galaxies. But the resultant diffuse emission is more than one order of magnitude

less than that observed in the Galactic and M31 bulges, indicating that gas in these bulges is in a subsonic outflow state probably due to additional mass loading to the hot gas and/or due to energy input rate that is substantially lower than the current estimate.

Subject headings: Galaxy: bulge — hydrodynamics — ISM: abundance — ISM: structure — supernova remnants: kinematics and dynamics

1. Introduction

Bulges of early-type spirals and elliptical galaxies comprise primarily old low-mass stars, which account for more than half of the total stellar mass in the local Universe (Fukugita, Hogan, & Peebles 1998). These stars collectively generate a long-lasting feedback via mass injection from evolved stars (mainly red giant branch stars and planetary nebulae) in the form of stellar winds and energy input from Type Ia SNe. Because of the SN heating, the ISM should be mostly in X-ray-emitting plasma inside galactic bulges, where little cool gas is present (e.g., Mathews & Baker 1971; Sage et al. 2007). Observations have shown that the X-ray-inferred gas mass and energy are far less than those empirical predictions (e.g., Sato & Tawara 1999; David et al. 2006). In other words, the bulk of stellar feedback expected is not observed (Wang 2007). This “missing” stellar feedback problem becomes particularly acute in so-called low L_X/L_B (i.e., the ratio of X-ray luminosity to blue band luminosity) bulge-dominated galaxies (typically Sa spirals, S0, and low mass ellipticals). After removing the contribution from point sources in those relatively deep *Chandra* observations, the remaining “diffuse” X-ray component generally shows a soft spectrum, indicating a thermal origin (Irwin et al. 2002; O’Sullivan et al. 2003), and its luminosity is only a few percent of the expected Type Ia SNe energy input (Li & Wang 2007; Li et al. 2007). The inferred total mass of the X-ray-emitting gas falls far short of what is deduced from the stellar mass loss over the galaxy’s lifetime (David et al. 2006).

The presence of a bulge-wide outflow may solve the “missing” stellar feedback problem (e.g. Tang et al. 2008). The 1D solution of an SN-heated bulge outflow, however, has problems. The physical state of the gas outflow mainly depends on the mass and energy input rates as well as the gravitational field. Within those low L_X/L_B galactic bulges of typical mass and energy input

rates, a hot bulge wind¹ should be present theoretically (e.g., Mathews & Baker 1971; Ciotti et al. 1991). However, observations of the diffuse hot ISM are apparently at odds with the theoretical wind models in nearly all aspects. Firstly, the predicted X-ray luminosity in a bulge wind scenario is a few orders of magnitude smaller than the observed (e.g., Tang et al. 2008). Secondly, the expected wind temperature is about ~ 1 keV or higher, while the observation-inferred gas temperatures are substantially lower (e.g., David et al. 2006; Li & Wang 2007). Thirdly, the estimated X-ray surface brightness profile of the wind should be steeper than that of starlight (Ciotti et al. 1991), but the observed profiles of diffuse emission distributions are fairly extended in most low L_X/L_B bulges or ellipticals (e.g. fig. 7 in Sarazin et al. 2001; fig. 5 in Li et al. 2007). Furthermore, the predicted mean iron abundance of the diffuse hot gas is 3–7 times solar because of the Type Ia SN enrichment (e.g., Ciotti et al. 1991; Sato & Tawara 1999), whereas the observed spectra usually indicate near- or sub-solar iron abundance.

Some, if not all, of the listed discrepancies may arise from various oversimplifications of the existing 1D models (e.g., Mathews & Baker 1971; White & Chevalier 1983; Lowenstein & Mathews 1987; Ciotti et al. 1991). In such models the mechanical energy input of SNe is always treated as pure thermal energy smoothly injected into the ISM. In reality, however, SNe, sporadic in both time and space, should naturally produce inhomogeneity in the ISM. The density and temperature inhomogeneity may significantly affect the X-ray spectrum and luminosity, which are proportional to the density square. Explosive energy injection in a hot tenuous medium can be transported away in form of sound wave, so the SN heating is not local (e.g., Tang & Wang 2005). Furthermore, whether or not the SN ejecta of each individual SNR can be well mixed with the surrounding material is crucial to address the apparent low abundance puzzle of the hot gas. These effects need to be quantified in order to correctly interpret the existing observations.

In this work, we present a pilot study to explore the properties of hot gas in galactic bulges by conducting 3D hydrodynamic simulations. In these simulations, SNe are randomly generated that statistically and spatially follow the stellar light distribution. Based on the mean temperature and density of the surrounding medium, we adaptively determine the appropriate sizes of individual SNRs and generate their density, temperature, and velocity profiles from a library of 1D simulated

¹Hereafter in our paper we use the term *wind* specifically for a supersonic outflow and *outflow* for an outflow in either supersonic or subsonic state.

SNR templates. We then plant such structured SNR seeds into the 3D simulation grid and let them evolve. We terminate the simulation when it reaches a statistically steady state. The 3D simulations not only provide us with the dynamical structures of SNRs, but also enable us to trace the thermal and chemical states of the bulge wind material.

The organization of the paper is as follows. In §2 we describe the main physical ingredients of the bulge wind model and the numerical methods. The results are presented in §3 and discussed in §4. We summarize our results and conclusions in §5.

2. Model and Method

2.1. Model Basics

We model hot gas inside a galactic bulge that originates from continuous stellar injection in the form of stellar winds, and is heated by sporadic Type Ia SNe. The dynamics of the hot gas is described by the following equations:

$$\frac{\partial \rho}{\partial t} + 2\nabla \cdot (\rho \mathbf{v}) = \dot{\rho}_*(r) + \dot{\rho}_{SN}(\mathbf{r}, t), \quad (1)$$

$$\frac{\partial \rho \mathbf{v}}{\partial t} + \nabla \cdot (\rho \mathbf{v} \mathbf{v}) + \nabla P = -\rho \nabla \Phi, \quad (2)$$

$$\frac{\partial \rho E}{\partial t} + \nabla \cdot [(\rho E + P)\mathbf{v}] = -\rho \mathbf{v} \cdot \nabla \Phi + S_{SN}(\mathbf{r}, t) + S_*(r) - n_t n_e \Lambda(T), \quad (3)$$

$$P = nkT \quad (4)$$

where ρ , \mathbf{v} , P , T , and E denote density, velocity vector, pressure, temperature, and total specific energy of the hot gas; and Φ is the gravitational potential field; n_t and n_e are the number density of ions and electrons; $n = n_t + n_e$ is the total number density; $\Lambda(T)$ is the normalized cooling function taken from Sutherland & Dopita (1993), assuming an optically thin plasma with solar abundance; $\dot{\rho}_*$ and S_* denote the mass and energy input from evolved stars. The mass and energy input from individual SNe, $\dot{\rho}_{SN}(\mathbf{r}, t)$ and $S_{SN}(\mathbf{r}, t)$, are explicitly expressed as a function of position and time.

We adopt parameters appropriate to the bulge of the Milky Way. The stellar mass distribution of the bulge follows the potential-density pair of the Hernquist profile (Hernquist 1990):

$$\Phi_{bulge}(r) = -\frac{GM_{bulge}}{r + r_s}, \quad \rho_{bulge}(r) = \frac{M_{bulge}}{2\pi} \frac{r_s}{r} \frac{1}{(r + r_s)^3}, \quad (5)$$

where r_s is the scale radius and M_{bulge} is the total mass of the bulge. Here we set the M_{bulge} and r_s to be $2.4 \times 10^{10} M_\odot$ and 0.42 kpc (e.g., Kent 1992; Zhao 1994; Blum 1995; Wolfire et al. 1995; Lepine & Leroy 2000). Other components of our Galaxy, such as the disk and dark matter halo, have only little effects on the gas dynamics within the Galactic bulge and are thus ignored in our simulations.

The stellar mass loss from evolved stars, $\dot{\rho}_*(r)$, follows the stellar mass distribution. The total stellar mass loss rate of the bulge ($\dot{M} = \int \dot{\rho} dV$) is constrained by current theoretical predictions and related observations, although the true value cannot be observed directly inside the bulge. It is inferred from our knowledge of the stellar population and evolution, together with observations of the mass loss of similar stars in the solar neighborhood. Estimates of the stellar mass loss rate may vary by more than a factor of two. Assuming a single stellar population with a standard Salpeter initial mass function, Ciotti et al. (1991) found that the stellar mass loss rate can be approximated as

$$\dot{M} = 0.25 L_{10} t_{10}^{-1.3} M_\odot \text{ yr}^{-1}, \quad (6)$$

where L_{10} is the current optical blue-band luminosity in units of $10^{10} L_{B,\odot}$ of the stellar population and t_{10} is its age in units of 10 Gyr. Adopting a blue-band luminosity of $2 \times 10^9 L_{B,\odot}$ (Cox 2000, p571) and an age of 10 Gyr for the bulge, we have $\dot{M} \simeq 0.05 M_\odot \text{ yr}^{-1}$. Maraston (2005, fig. 22) directly relates mass loss to the total mass of a stellar population (see also Tang et al. 2008), which gives $\dot{M} \simeq 0.07 M_\odot \text{ yr}^{-1}$. Another estimate based on observations of asymptotic giant branch stars gives $\dot{M} = 0.64 L_{10} M_\odot \text{ yr}^{-1}$, consistent with the stellar mass loss rate inferred for a sample of nine ellipticals from mid-IR observations (Athey et al. 2002). Thus, \dot{M} for the Galactic bulge can be as high as $0.13 M_\odot \text{ yr}^{-1}$. We therefore run models with different mass loss rates, as discussed in §2.3.

The energy feedback of the stellar bulge is dominated by the mechanical energy from Type Ia SNe. Following the convention, we assume that each SN releases 10^{51} ergs mechanic energy. We take the Type Ia SN rate of E-S0 galaxies to be 0.12 SNU (SNU is defined as one SN per $10^{10} L_{B,\odot}$ per century; Cappellaro et al. 1999; Cox 2000, p467), which gives about one SN per 3000 year in our Galactic bulge. The energy input from the stellar wind, $S_*(r)$, is assumed to be thermalized to their stellar kinematic temperature $T_* \equiv \mu m_p \sigma^2 / 3k \simeq 3 \times 10^5 \text{ K}$, corresponding to a stellar velocity dispersion around 100 km s^{-1} (Eckart et al. 1993). Overall this energy is almost

negligible compared with that from SNe.

Each SN also ejects an adopted (Chandrasekhar) mass of $1.4 M_{\odot}$. Though the total amount of SN ejecta is much less than that of the mass loss from evolved stars, the SN ejecta contribute most of the metals, especially iron. In order to trace how these iron-rich ejecta mix with the stellar wind material, we additionally incorporate a separate advection equation

$$\frac{\partial \rho \chi_i}{\partial t} + \nabla \cdot (\rho \chi_i \mathbf{v}) = 0, \quad (7)$$

where χ_i is the mass fraction of the i th component, with the constraint $\sum_i \chi_i = 1$. In the present simulations we have two components, the iron mass and the rest of gas mass. The iron mass from SNe, assumed to be $0.7 M_{\odot}$ per SN (Nomoto et al. 1984), is part of the SN ejecta. The iron mass fraction in stellar wind material is $f_{Fe, \odot} = 0.1\%$ (i.e., the nominal solar). The iron abundance can trace the SN enrichment. Any zone with iron abundance greater than the solar value is enriched by SNe. Thereafter we refer the iron ejecta as purely from SNe.

The simulations are performed with FLASH (Fryxell et al. 2000), an Eulerian astrophysical hydrodynamics code with the adaptive mesh refinement (AMR) capability, developed by the FLASH Center at the University of Chicago. FLASH solves the Euler equations and uses the piecewise-parabolic method to deal with compressible flows with shocks. We take the advantage of the AMR capability to accurately include the heating of individual SNRs.

2.2. One Dimensional Model

To help set up the 3D simulations, we first simulate a 1D model. Assuming that the energy and mass inputs are continuous in time and spherically symmetric in space, we may simplify Eqs. (1)–(3) into a 1D problem. For a specific galactic bulge, the *crossing time*—the time required for the gas to flow from the center to the outer boundary—is a few million years (assuming a size of a few kpc for the bulge), significantly shorter than the evolutionary time scale of the stellar energy and mass input rates. Therefore, the problem can be regarded as time-independent. The bulge outflow can reach a steady state if radiative cooling does not affect the dynamics.

We run the 1D simulations by using a gas-free initial condition and by continuing to add corresponding energy and mass in each zone. FLASH handles the mass and energy inputs with

an operator split method. At each time step it first solves the Eulerian equations without the source terms, then explicitly updates the solution to account for the corresponding source terms. To properly conserve the mass, momentum, and energy, we implement this procedure in three steps: first, we update the gas density according to the amount of mass input in that step; next, we modify the gas velocity to satisfy momentum conservation; finally, we modify the gas temperature to conserve the total energy. We verified that this implementation can exactly produce the analytical solution of a star cluster wind (Canto et al. 2000).

The system eventually evolves to a steady state. Such a steady outflow solution can be analytically derived without including cooling (White & Chevalier 1983). If the 1D bulge outflow solution has a sonic point, a subsonic outflow can then develop into a supersonic outflow (i.e., a bulge wind). The final state of such a wind does not depend on the specific initial condition. Under certain conditions (e.g., due to significant radiative cooling or low specific energy input; see §4.2 for more discussion), the sonic point may not exist and the gas outflow may be sensitive to the boundary condition as well as the initial condition. The use of the outflow (sometimes called zero-gradient) boundary condition would then introduce an artificial force inserted by the leveled-off pressure that would produce perturbation, propagating inwards on a time scale comparable to the crossing time. This situation would also occur if a simulation region were too small to include the sonic point (if present). Thus we use the 1D solution to make sure that the sonic point is included in the 3D simulation domain (a cubic box).

2.3. Three Dimensional simulations

Two 3D simulations are performed to examine the properties of galactic bulge winds. Their key parameters are listed in Table 1 for quick reference. The major difference between these two simulations is the mass loss rate: $0.05 M_{\odot} \text{ yr}^{-1}$ for Model A (the 3D reference model) and $0.1 M_{\odot} \text{ yr}^{-1}$ for Model B, representing the uncertainty in the mass loss rate (§2.1) or extra mass loading expected in galactic bulges (§4.2; see also Li & Wang 2009 in preparation). The highest spatial resolutions are ~ 3.9 and 4.9 pc respectively for the two models. The effective single-grid resolution of the simulations are 1024^3 and 2048^3 zones. The steady wind flow established in the 1D model is used as the initial flow with an iron mass fraction of the solar value ($f = 0.1\%$).

In the 3D realizations, SNe explode randomly according to a Poisson process with the mean overall rate. Their spatial distribution statistically follows the stellar density distribution. It would be computationally very expensive, if even possible, to simulate the evolution of each SNR on sub-parsec scales within the bulge-wide flow. Instead, we adaptively plant individual structured SNR seeds into the 3D simulation grid and then let them evolve. We do not simply adopt the Sedov solution, which is generally not appropriate for an SNR evolving in a hot tenuous medium (Tang & Wang 2005), especially when the dynamics of the SN ejecta are considered. According to a scaling scheme detailed in a separate paper (Tang & Wang 2009), the structure of an SNR can be scaled from a template SNR simulated in a different ambient medium setting. We have constructed a library of template SNRs from 1D simulations, assuming a selection of ambient gas temperatures and densities. Each entry of this library consists of the density, temperature, and velocity profiles at a particular age and a forward shock radius.

We apply the scaling scheme to dynamically generate the profiles of each SNR seed. Specifically, we select a spherical region around each SN location within which the density and pressure are sufficiently smooth, using the Löner’s error (FLASH User’s Guide; Löner 1987) as the estimator. We find that at least 500 zones (i.e., more than 5 points for the radial profiles) are needed to reasonably well represent a structured SNR seed. This in turn requires the minimum embedding radius to be at least 20 pc, given the spatial resolution that is achievable in our simulations. With the embedding radius determined, we calculate the mean density and gas-mass-weighted temperature of the enclosed gas to find the most suitable template in the library and to form the required SNR seed (Tang & Wang 2009).

The planting of an SNR seed also takes a few steps. First we refine the affected region to the highest refinement level. Then we normalize the SNR structures to ensure the conservations of mass, momentum, and energy within that region (see Appendix A for details). Finally, the innermost region that encloses $0.7 M_{\odot}$ is traced as the pure iron ejecta of the embedded SNR. This embedding procedure is well parallelized and allows for linear scaling up to at least 1024 processors.

To save computing time, one may simulate only one octant of the bulge by adopting a reflecting boundary condition at the surfaces across the center. A test run, however, shows that a reflecting boundary condition introduces correlated wave interactions when an SN explodes near the reflecting boundaries. This effect is not physical and difficult to quantify. It is most serious near the bulge

center where three reflecting boundaries intersect and the stellar density, hence the rate of the SNe, is the highest. Thus we resort to simulating the whole bulge, which is centered inside the simulation domain. However, we only simulate one octant at full resolution, while the highest resolution in the rest of the grid is degraded by a factor of four, except for regions where SNRs seeds have just been embedded. These regions are forced to have the full resolution in all octants, and are held for 10^5 years before returning to the default AMR. We use refinement estimators acting on the density and pressure to determine whether a block needs to be refined or derefining, adopting the default criterion suggested (in FLASH User’s Guide, i.e., refining a block if any estimator is greater than 0.8 and derefining it if all estimators are less than 0.2). Regions outside the sonic radius (which is obtained from the 1D model) are allowed to have a lower refinement level that gradually decreases with radius. This approach circumvents the reflection boundary problem at the expense of about 60% more computing time, which is acceptable. In addition, it allows us to examine the resolution effect within a single run.

A statistically steady state of such a 3D simulation can be reached after a few crossing times. We quantify the establishment of the steady state of a 3D bulge wind by examining the relative variation of its global quantities such as the total mass and energy. Here we define the variation as the change of a given quantity relative to its initial value, i.e., the relative difference between 3D and 1D. The variation of the total mass within 2.0 kpc of Model A is shown in Fig. 1a by the solid line. Compared to its initial value, the total mass increases to $\sim 7\%$ on average and fluctuates around this value with a period of ~ 10 Myr, comparable to the flow crossing time. As expected, the mass variation within the inner 1.2 kpc radius, displayed as the dashed line in the figure, has a shorter fluctuation period. The expected iron mass fraction, if fully mixed with stellar wind material, is 0.35% (~ 3.5 times the solar abundance) in Model A. We show the variation of the

Table 1. Model Parameters

Model	\dot{M} ($M_{\odot} \text{ yr}^{-1}$)	\dot{E}_{sn} ($10^{40} \text{ ergs s}^{-1}$)	r_{sonic} (kpc)	ΔL (pc)	L (kpc)
A	0.05	1.1	1.0	3.9	4
B	0.1	1.1	1.8	4.9	10

iron abundance (in the solar units) in Fig. 1c. It takes about 5 Myr for the hot gas inside 2 kpc to gain the expected iron mass. The variation of the iron abundance is smaller than that of total mass, mainly because it actually only reflects the ratio of total iron mass to the total gas mass. By introducing random SN events in the 3D simulations, the globally conserved quantities are no longer constant as they should be in a 1D spherical steady flow. Only when a hydrodynamic steady state is established in the simulations (i.e., the fluctuation has reached a statistically stable level) is the comparison between 1D and 3D results meaningful.

We check the resolution effect based primarily on X-ray luminosity, which is particularly sensitive to the density structure in the simulations. We find that the X-ray luminosity difference between the high resolution octant and the other seven octants is rather small. This is partly because the majority of the emission arises from individual SNRs which are resolved at the same resolution in all the octants. To examine the resolution effect more directly, we resume Model A with an increased spatial resolution by a factor of two, and let it only evolve for 0.1 Myr, limited by the available computing time. This simulation produces finer structures of the bulge gas, and the resultant X-ray luminosity increases about 3% in the high resolution octant and about 10% in the other seven octants. This demonstrates that our results are quite robust and are only slightly affected by the spatial resolution.

3. Results

In this section we present the gas properties extracted from the 3D hydrodynamical simulations. We first detail the results of Model A (Fig. 2) and then present Model B (Fig. 3) for comparison. Data near the outer region are excluded in our analysis to avoid any potential artifacts introduced by the assumed outer boundary condition of the simulations. We show time-dependent gas properties such as global structures, individual SNRs, and X-ray luminosities as well as various time-averaged measurements. The average is made over a time span ranging from 15 to 30 Myr, when the simulations have reached quasi steady states (see Fig. 1).

3.1. Structures

Fig. 2 shows snapshots of the simulated density, temperature, pressure, and iron ejecta mass fraction of Model A in the $z = 2$ pc plane. Sporadic SN events produce non-uniformity in the bulge wind. The prominent features are various shell-like and filamentary density structures. These shell-like structures of SNRs are easily identified in the outer region, where the explosions are less frequent and each SNR can evolve individually to a large volume before colliding with others. Individual SNRs near the bulge center appear more compact because of the high gas density and pressure and frequent interactions with adjacent remnants. Evolved remnants tend to be dispersed and advected outward. Higher temperature regions in general represent low-density interiors of SNRs. The distribution of the pressure is much smoother than those of the density and temperature (Fig. 2d), as has also been found for the SN driven ISM in the Galaxy (de Avillez & Breitschwerdt 2005; Mac Low et al. 2005; Joung & Mac Low 2006) and in starbursts (Joung et al. 2008). The shell-like structures in the pressure map correspond to the expanding blastwaves. Inside each SNR, the pressure is nearly uniform, as expected from the Sedov (1959) solution. The spatial distribution of iron ejecta is far from uniform, as illustrated in Fig. 2c. Regions with the lowest iron mass fraction are primarily filled with stellar wind material with little mixing with the iron ejecta. Gas with an intermediate iron mass fraction represents iron ejecta diluted by constantly injected stellar wind material (or mildly by numerical mixing). Though being diluted and fragmented, the iron ejecta is advected out of the bulge, hardly mixing with the bulk of stellar wind material. Hence, the ISM is not uniformly enriched by SN ejecta within the bulge. Similar results are also present in Model B (see Fig. 3).

Fig. 4 shows sample density, temperature, and velocity profiles of the hot gas at two representative times. Individual troughs shown in the density profiles represent interiors which are surrounded by peaks (i.e., expanding shells of SNRs). The temperature profiles are nearly anti-correlated with the density profiles: a peak in temperature usually corresponds to a trough in density at the same locus, which is equivalent to the smooth pressure profiles (e.g., Mac Low et al. 2005; Joung & Mac Low 2006). As SNRs evolve, the loci of peaks and troughs change with time. Multiple evolved SNRs appear to be wave-like. This wave-like flow driven by sporadic SNe produces the fluctuations in the globally conserved quantities (Fig. 1).

We demonstrate the evolution of a few SNRs (labeled as I, II, and III) very close to the bulge

center in Fig. 5 taken from the high resolution study. The forward blastwave of SNR I is evident in the density panel at 10^3 year. The pure iron core has a radius of about 10 pc at this time. The blastwave expands faster toward the lower-right region, where a lower density cavity has been created by an earlier SNR (labeled as II). SNR I is unusual in that it occurs right at the bulge center. Because of the high stellar wind injection rate there, its iron ejecta are diluted quickly. SNRs away from the center are less affected by the stellar wind dilution. SNR II, for example, at an age of 2×10^4 year still has an iron mass fraction of $\sim 6\%$, corresponding to 60 times the solar abundance. The collision between SNR I and II is also evident in the lower-right subpanel of each group. The evolved shapes of these SNRs are asymmetric because of both the inhomogeneous environment and interactions with other SNRs.

3.2. Time-Averaged Distributions

Fig. 6 shows the time-averaged gas mass and volume distributions in the high resolution octant as functions of temperature and density in two regions: $0 < r < 0.6$ kpc and $0.6 < r < 1.2$ kpc. The distributions in both regions are broad. As expected, the mass distribution is biased toward the lower temperature and higher density side relative to the volume distribution. Relatively cold dense gas (e.g., distributed in the upper-left corner of Fig. 6a) occupies negligible volume, lying outside the 1% contour level of the gas volume distribution. To see the results more quantitatively, we show their marginal distributions in temperature and density respectively (Fig. 7). The volume distribution resembles a power law with an index of roughly -2 at the high-temperature end. The mass distribution is similar to the volume distribution but peaks at a lower temperature.

Fig. 8 shows the differential emission measure (EM) as a function of temperature within a radius of 1.2 kpc. The EMs from the low- and high-resolution regions are nearly identical around the peak value. The bulk of the broad EM distribution, peaked at $\sim 3.7 \times 10^6$ K, can be approximated by a log-normal distribution, with small deviations mostly at the high temperature end. The grey region in the figure encloses the 50% intervals below and above the mean of the whole region.

3.3. X-ray Emission and Spectra

We calculate the luminosities and spectra using the standard software package XSPEC based on the EM distributions. For the hot gas considered here, we adopt the standard MEKAL model (Mewe et al 1985; Liedahl et al. 1995) for plasma in collisional ionization equilibrium. Fig. 9 shows a synthesized spectrum of Model A assuming a solar abundance. The luminosities in a few bands of Model A are listed in the 4th row of Table 2. The corresponding spectra and luminosities of Model B are presented in Fig. 9 and in Table 2 as well. The luminosity of Model B in the low energy band increases dramatically; e.g, in the 0.2-0.5 keV band it is more than 60 times larger than that of Model A. This increase is due to the combination of higher density and lower temperature (hence higher emissivity) of the weak bulge wind (see §4.2 discussion). Of course, the X-ray emission depends on the metal abundance as well. If an abundance expected for stellar material fully mixed with SN ejecta were adopted, the luminosities in the three bands would increase by a factor of a few, as listed in Table 2.

Since the iron ejecta are in fact not well mixed with the surrounding material, we examine the effect of the non-uniform metal distribution on X-ray emission. The normalized EM distribution as a function of the iron abundance is plotted in Fig. 10 as the solid black line. It shows that about 80% of the EM comes from the material with the iron abundance less than 1.5 times solar. The corresponding distribution of the luminosity in the 0.3-2 keV band nearly follows that of the EM. But the distribution of the luminosity in the 2.0-5.0 keV band is affected considerably by gas with higher iron mass fractions (corresponding to SNR interiors that in general have higher temperatures). Thus the majority of the X-ray emission from the bulge wind comes from the stellar wind material that is hardly enriched by SNe ejecta. In the following, we thus adopt the solar abundance for our calculations.

Fig. 11 shows the time variation of the 0.3-2.0 keV luminosity of Model A in two concentric regions: an inner region with $r < 0.6$ kpc, and an outer region with $0.6 < r < 1.2$ kpc. The luminosity in the inner region has a larger fluctuation (up to a factor of 3) than that in the outer region. The X-ray emission from the region with $r > 1.2$ kpc is negligible. The total 0.3-2.0 keV X-ray luminosity is only $\sim 10^{36}$ ergs s⁻¹ with a fluctuation less than a factor of two. Thus overall the X-ray emission of the diffuse gas is not significantly affected by the sporadic SN heating.

Fig. 12 illustrates the 0.3-2.0 keV surface brightness profile at several representative times. The brightness varies by more than an order of magnitude near the center. Compared with the stellar surface density profile (gray line), the X-ray profiles are generally steeper. Fig. 13 shows the X-ray surface brightness maps in three representative bands (0.3-0.7, 0.7-2.0, and 2.0-5.0 keV). The maps in the two lower energy bands do not show significant structures; those small features are typically not associated with individual SNRs. In the 2.0-5.0 keV map, individual SNRs are recognizable because they are the primary source of the hard X-ray emission.

3.4. Energy Distribution

From the 3-D realization, we can further quantify the thermal, kinetic energies as well as the turbulent motion of the hot gas. Fig. 14 shows the distributions of kinetic and thermal energies as a function of temperature at four different regions. The energy distribution peaks at 5×10^6 K. At temperature below 5×10^6 K, the energy is dominated by the thermal energy near the center ($0 < r \leq 0.4$ kpc), while the thermal and kinetic energies contribute almost equally at large radii ($r > 1.2$ kpc). Note that for ideal gas with the ratio of specific heat $\gamma = 5/3$, the Mach number is 1.34 (i.e., supersonic flow) when its thermal energy equals to its kinetic energy. The thermal energy of much hotter gas, primarily low-density hot SNR ejecta, is always much larger than its kinetic energy, which means that the SNR ejecta leave the simulation region subsonically. The difference between the total kinetic energy and its radial component reveals the energy contained in non-radial motion. Inside the scale radius ($0 < r \leq 0.4$), $\sim 30\%$ of the kinetic energy is in non-radial motion. This fraction is less than 2% in the outer shell ($1.2 < r \leq 1.6$). As a whole, $> 80\%$ of the thermal and kinetic energy of the bulge wind is stored in gas with temperature between $10^{6.5}$ K to $10^{7.5}$ K. The hotter gas ($T > 10^{7.5}$ K) contains $< 5\%$ of the total energy.

4. Discussions

4.1. Comparison between the 1D Model and 3D Simulation

Fig. 15 compares averaged radial profiles for the density, temperature, velocity, and pressure in a few snapshots of Model A with the corresponding 1D results. The velocity and pressure profiles averaged in radial bins follow the 1D results excellently. In the 3D simulation there is no unique

location of the sonic point to divide the supersonic flow from subsonic flow since the velocities and temperatures vary greatly from point to point. Nevertheless, the average hot gas outflow does become supersonic at ~ 1.0 kpc, close to the 1D sonic point (marked by the arrow). The density and temperature profiles deviate significantly from the corresponding 1D results in the inner region ($r < r_s$). In particular, the density profile tends to be more centrally peaked in the 3D simulations. This temporary accumulation of stellar wind material is largely due to the continuous mass injection and the lack of prompt heating. The variation of the density profiles, especially near the center, is closely coupled with the realization of SN events. At large radii the density and temperature profiles become nearly identical to the 1D results. Since the radiation of the bulge wind is negligible, the identical radial profiles at large radii are expected due to the conservation of mass and energy. Thus the nature of sporadic SN explosions does not affect the overall gas dynamics on large scales. In Fig. 16 we compare the profiles of the octant at full resolution to profiles of three low resolution octants. The figure suggests that the profiles show numerical convergence at a level better than the random variance among realizations.

On average the gas temperature in the 3D simulation has a lower and flatter profile than that in the corresponding 1D result. In the 1D model, the gas temperature is the highest at the center and decreases outwards monotonically. In contrast, the average gas temperature in a 3D simulation can be much lower at the center than in the surroundings, because of non-uniformly distributed SN heating. The distribution of SN heating depends on the ambient medium. An SN that explodes in a dense environment like the bulge center, heats a small region to a rather high temperature. The small amount of overheated gas advects outward and carries a large fraction of the SN energy with it, while leaving much of the central gas unheated. The unheated gas accumulates around the bulge center, resulting in a relatively steep density profile near the bulge center (see Fig. 15 panel a). The large density gradient makes it even harder for the SN heating to be uniformly distributed near the center, so it tends to be transported to outer low density regions (see also Hnatyk & Petruk 1999). Thus a low-temperature inner region naturally forms under the sporadic SN heating scenario.

It is also worth noting that the temperature profile depends on the weighting methods, as shown in Fig. 17. The EM-weighted value, which closely resembles that inferred from X-ray observations, is relatively low because it is primarily determined by the low-temperature denser material (see §3.2). In comparison, the temperature profiles from different weighting methods are identical in

the 1D model. This is because in the 1D model, all quantities such as temperature, density, and pressure are monotonic functions of radius. Therefore the density has a one-to-one correspondence to the temperature, which also explains the single-line gas distribution of the 1D model in the temperature and density space (Fig. 6).

The integrated gas properties of Model A are also significantly different from those of the 1D model, such as the EM distributions, spectra, X-ray luminosities, etc. In the 1D model the EM peaks at $\sim 8 \times 10^6$ K and is truncated sharply at low or high temperatures (three-dots-dashed magenta line in Fig. 8), while the EM distribution of Model A peaks at a lower temperature and is much broader. But the difference between the spectral shape of Model A and the corresponding 1D model is small in the 0.7-3.0 keV band (see Fig. 9). Model A has slightly higher (about 30% more) X-ray luminosity in this band. At lower (< 0.7 keV) and higher energy bands (> 3.0 keV), Model A gives much higher photon fluxes, especially for some line features, such as OVII (22.0\AA , 0.56 keV) and helium-like iron $K\alpha$ (FeXXV $K\alpha$; 6.7 keV), largely due to the much broader temperature distribution. It is worth noting that the FeXXV $K\alpha$ line emission in Model B increases but the line in its corresponding 1D model is missing because of the relatively low and narrow gas temperature distribution in the 1D model.

4.2. Observational Implications

There are two direct predictions from the 3D simulations that help to understand partly the observational puzzles faced by the 1D wind model. First, the relatively low emission-weighted gas temperature is consistent with the results inferred from the diffuse X-ray emission in galactic bulges and elliptical galaxies (e.g, Sarazin et al. 2001; David et al. 2006; Li & Wang 2007). Second, the SN Ia ejecta are not fully mixed with the stellar wind material inside the galactic bulge, and most of the X-ray emission is contributed by the stellar wind material shocked by SN blastwaves. Thus the X-ray spectra in general reflect only the metal abundance of the stellar wind material, which is consistent with the apparent solar metallicity inferred from the diffuse X-ray emission in a large sample of ellipticals (e.g., Humphrey & Buote 2006).

In addition, the broadening of the gas temperature distribution can also affect the determination of metallicity. A low metal abundance could be obtained by fitting the X-ray spectra of such

gas with an isothermal plasma model. This effect is demonstrated in Fig. 18. We simulate the X-ray spectrum based on the MEKAL model in XSPEC, adopting the approximate log-normal EM distribution (see §3.2) and a solar abundance. The data points in the upper panel show a simulated spectrum of about 600 photons. If we fit this simulated spectrum with a single-temperature MEKAL model, the resulting abundance is only about half solar (0.49 ± 0.17). The fit is statistically acceptable (with $\chi^2 = 42.4/41$), partly due to the small counting statistics. If the simulated spectrum contains 10^4 photons instead, the fit is no longer acceptable (with $\chi^2 = 213/91$) and the best fit tends to give a much lower abundance (about one-third solar). A two-temperature component model can significantly improve the fit, and the abundances are in general less than one solar, although they are not strongly constrained. Thus the abundance is likely underestimated by fitting an X-ray spectrum of gas with broad temperature and density distributions (see also Strickland & Stevens 1998).

Given the low resolution and small signal-to-noise ratio of X-ray spectra typically available for diffuse hot gas, it is difficult to distinguish gas with a broad temperature distribution from an isothermal plasma, especially within a narrow energy band. In Fig. 9 we plot an arbitrarily normalized spectrum of a single-temperature hot plasma (0.8 keV for Model A and 0.4 keV for Model B, where the EM distribution of the corresponding 1D model peaks). The spectra of the 3D simulation and the isothermal plasma model are similar in the 0.5–2.0 keV band. This approximation gives a potential shortcut to fit the X-ray observations coarsely with only one or two gas components, which are not necessarily able to reveal the actual physical and chemical state of the ISM. With higher resolution spectra, line diagnostics may provide additional useful information to reveal the gas properties.

However, the models still predict far lower X-ray luminosities than observed. The observed diffuse X-ray luminosity in the 0.5–2 keV band of our Galactic bulge and M31 bulge is about 10^{38} ergs s^{-1} (Shirey et al. 2001; Takahashi et al. 2004; Munro et al. 2004; Li & Wang 2007). Using the reference mass and energy input rates, the bolometric X-ray luminosity predicated by the 1D wind model is no more than 10^{36} ergs s^{-1} . The inhomogeneous structures of the gas density and temperature in Model A increase by no more than half an order of magnitude the luminosity in the 0.5–2 keV band (Table 2). This under-prediction of the observed luminosity remains a serious problem for the models.

The parameter with the strongest influence on the luminosity of the bulge wind is the stellar mass loss rate. As demonstrated in Model B which has a doubled mass input rate, its mean gas density increases while the temperature decreases. The X-ray emission increases by a factor of ~ 20 in the 0.5-2.0 keV band. This enhancement is due to the increase of both density and emissivity. To quantitatively understand this trend, let us first consider a scaling relation of the bulge wind. The specific heating $\beta = \dot{E}/\dot{M}$ determines the mean central gas temperature of the wind solution. In a steady flow, the velocity $u \propto \beta^{0.5}$ (e.g. White & Chevalier 1983), so long as gravitational potential energy remains unimportant. We have $\rho \propto \dot{M}\beta^{-0.5}$ from the mass conservation equation, and $T \propto \beta$ from the energy conservation equation. For gas with a temperature between 0.5 and 1.0 keV, the X-ray emissivity in the 0.5–2.0 keV band is roughly inversely proportional to the temperature [e.g., $\Lambda(T) \propto T^{-0.7}$ based on the MEKAL model]. The total X-ray emission is then $L \propto \rho^2 \Lambda(T) \propto \dot{M}^{3.7} \dot{E}^{-1.7}$. For winds with the same β the velocity and temperature profiles are the same, and density profiles differ only in their normalization, which is proportional to \dot{M} . We thus use β/β_* to denote the separate change of either \dot{M} or \dot{E} , e.g. $L \propto \dot{M}^{3.7}$ is equivalent to $L \propto (\beta/\beta_*)^{-3.7}$ for a fixed energy input, and $L \propto \dot{E}^{-1.7}$ to $L \propto (\beta/\beta_*)^{-1.7}$ for a fixed mass input. Fig. 19 shows the luminosity in the 0.5–2 keV as a function of β based on a suite of 1D simulations. In this plot the luminosities are normalized to that of a 1D reference model ($L_* \sim 10^{36} \text{ergs s}^{-1}$; corresponding to Model A). The scaling relations of L versus \dot{M} and \dot{E} closely match the simulations when β/β_* is larger than 0.5. In the adopted galactic bulge, if the specific energy approaches one-third of the reference value, the simulated luminosities increase sharply and no longer follow the scaling relation, because the gravitational potential becomes dynamically important for such a small β . The corresponding results of Models A and B are also plotted in Fig. 19 to show the effects of gas inhomogeneity. The ratio of the 0.5-2.0 keV luminosity of Model A to that of the corresponding 1D model is about 2, and the ratio is about 3 for Model B.

Let β be fixed at the reference value in Model A, the velocity and temperature profiles of the wind should remain the same and $L_X \propto \dot{M}^2$. Hence, both \dot{E} and \dot{M} need to increase by an order of magnitude in order to boost the X-ray luminosity to match that observed in the M31 bulge. Although a bulge wind with a reduced β can significantly increase the diffuse X-ray emission as demonstrated in Model B, it is unlikely to be the best solution. In the presence of a reasonable dark matter halo with properties like that of the Milky Way galaxy (e.g., $M_{halo} \simeq 10^{12} M_\odot$, $r_{virial} \simeq 250 \text{ kpc}$, an NFW profile with a concentration parameter of 15), $\sim 120\%$ of the available energy

input in Model B is required for the escape of all the stellar ejecta to beyond the virial radius. Thus the bulge wind in Model B is not energetic enough to escape the galaxy potential well and the bulge wind material must accumulate within the virial radius. This accumulated material may form a considerable circum-galactic medium (CGM) that could eventually quench the bulge wind (Tang et al. 2008).

The gas outflow might be subsonic in the vicinity of galactic bulges and other ellipticals with low L_X/L_B ratios under the interaction between the bulge wind and CGM. The subsonic state is necessary to explain both the large luminosity (compared to the wind model prediction) and the extent of the diffuse X-ray emissions. Even if a bulge wind has the energy to escape the halo virial radius, the wind can be reversely shocked and stalled by the CGM. When the reverse shock propagates inward within the sonic point, the bulge wind turns into a globally subsonic outflow. Such a subsonic state can be quasi stable for a long time with proper treatment of the boundary the galactic flow (Tang et al. 2008). A proper 3-D simulation including the entire CGM is possible, though computationally very expensive at present.

Other effects, which are ignored here for simplicity, can further affect the X-ray luminosity of the galactic bulges. A vertically collimated bulge wind can be a promising way to significantly boost the X-ray luminosity, particularly for objects such as M31 with a considerable mass in the galactic disk. Motivated by the observed bipolar diffuse X-ray emission in the M31 bulge (Li & Wang 2007), we have found in preliminary simulations that a vertically collimated wind, confined by the surrounding gaseous disk, will have significantly higher X-ray emission (by up to an order of magnitude). The major reason is that the density diverges much slower in the collimated wind than in the spherical wind. We plan to address this issue in a separate paper (Tang & Wang in preparation).

5. Summary

In this work, we have explored the properties of the structured hot gas created by sporadic SN explosions inside a galactic bulge by conducting detailed 3D hydrodynamical simulations. Our main results are as follows:

- A galactic wind may be generated in a galactic bulge with the standard empirical stellar mass loss and Type Ia SN rate. The gas properties fluctuate in time particularly in the central region lying within the sonic radius of the wind, where individual SN explosions strongly influence the density and temperature distributions. At larger radii, the spherically average profiles of the 3D simulations follow those of the 1D models. Therefore the 1D treatment of a galactic bulge wind flow is a reasonable approximation on large scales.
- Sporadic SN explosions produce 3D filamentary and shell-like structures in the gas. These structures result in broad density and temperature distributions, compared to the 1D model. Furthermore, the relatively low temperature of the structures leads to an emission measure-weighted temperature that is significantly lower than the expected value inferred from the specific heating and has a relatively flat radial distribution throughout the bulge region, consistent with observations.
- Iron ejected by SNe does not mix well with the surrounding gas within the bulge region and has a relatively high temperature and low density, so it contributes primarily to emission in the energy band > 2 keV. The diffuse soft X-ray emission comes from shells associated with SN blastwaves, which are hardly enriched by SN ejecta and have a metallicity close to the ambient gas that originates in stellar winds. This, together with the temperature broadening, helps to explain the apparent sub-solar abundance of the soft X-ray-emitting gas in galactic bulges/ellipticals.
- Compared with the 1D spherical wind model, the structured hot gas in 3D simulations can boost the X-ray emission in an intermediate energy band (e.g., 0.5-2.0 keV) by a factor of a few. This increase is more significant at the lower or higher energy bands due to the broad distributions of both temperature and density. In order to produce the luminosity and surface brightness distribution similar to the observed diffuse X-ray emission, the bulge outflow likely needs to be in a subsonic state and/or an angularly confined configuration.

Acknowledgments

The software used in this work was in part developed by the DOE-supported ASC / Alliance Center for Astrophysical Thermonuclear Flashes at the University of Chicago. Simulations were

performed at the Pittsburgh Supercomputing Center supported by the NSF. This project is supported by NASA through grant SAO TM7-8005X and NNG07AH28G.

REFERENCES

- Athey A., Bregman J., Bregman J., Temi P., Sauvage M., 2002, *ApJ*, 571, 272
Borkowski K. J., Lyerly W. J., Reynolds S. P. 2001, *ApJ*, 548, 820
Blum, R. D. 1995, *ApJ*, 444, L89
Canto J., Raga A. C., Rodriguez L. F., 2000, *ApJ*, 536, 896
Cappellaro E., Evans R., Turatto M. 1999, *A&A*, 351, 459
Ciotti L., Pellegrini S., Renzini A., & D’Erocole A. 1991, *ApJ*, 376, 380
Cox A. N., 2000, *Allen’s Astrophysical Quantities*, fourth edition.
David L. P., Jones C., Forman W., Vargas I. M., Nulsen P., 2006, *ApJ*, 653, 207
de Avillez M. A., & Breitschwerdt D., 2005, *A&A*, 436, 585
Eckart A., Genzel R., Hofmann R., Sams B. J., Tacconi-Garman L. E., 1993, *ApJ*, 407, L77
Fryxell B., et al., 2000, *APJS*, 131, 273
Hernquist L. 1990, *ApJ*, 356, 359
Hnatyk B., Petruk O. 1999, *A&A*, 344, 295
Humphrey P. J., & Buote D. A., 2006, *ApJ*, 639, 136
Irwin, J. A., Sarazin, C. L., Bregman. J. N. 2002, *ApJ*, 570, 152
Joung M. K., & Mac Low M.-M., 2006, *ApJ*, 653, 1266
Joung M. K., Mac Low M.-M., Bryan G. L., 2008, *astroph/arXiv0811.3747*
Kent S. M. 1992, *ApJ*, 387, 181
Lepine J. R. D. & Leroy P. 2000, *MNRAS*, 313, 263
Li Z., Wang Q. D., 2007, *ApJ*, 668, L39
Li Z., Wang Q. D., Hameed S. 2007, *MNRAS*, 376, 960
Liedahl D. A., Osterheld A. L., & Goldstein W. H., 1995, *ApJ*, 438, L115
Lowenstein M., & Mathews W. 1984, *ApJ*, 319, 614
Löhner R. 1987, *Comp. Meth. App. Mech. Eng.*, 61, 323
Mac Low M.-M., Balsara D. S., Kim J., de Avillez M. A., 2005, *ApJ*, 626, 864
Maraston C. 2005, *MNRAS*, 362, 799
Mathews W. G. & Baker J. C. 1971, *ApJ*, 170, 241
Mewe R., Gronenschild E. H. B. M., & van den Oord G. H. J. 1985, *A&AS*, 62, 197
Muno M. P., et al., 2004, *ApJ*, 613, 326
Nomoto L., Thielemann F., & Yokoi L. 1984, *ApJ*, 286, 644
O’Sullivan E., Ponman T. J., Collins R. S. 2003, *MNRAS*, 340, 1375

- Sage L. J., Welch G. A., Young L. M. 2007, *ApJ*, 657, 232
- Sarazin C. L., Irwin J. A., & Bregman J. N. 2001, *ApJ*, 556, 533.
- Sato S., & Tawara Y. 1999, *ApJ*, 514, 765
- Sedov L. I 1959, *Similarity and Dimensional Methods in Mechanics*, translation from 4th Russian edition, Academic press New York and London
- Shirey R., et al., 2001, *A&A*, 365, L195
- Shu F. H. 1992, *The physics of astrophysics, Volume II, Gas Dynamics* (University Science Books)
- Strickland D. K., & Stevens I. R., 1998, *MNRAS*, 297, 747
- Sutherland R. S., & Dopita M. A., 1993, *APJS*, 88, 253
- Tang S., & Wang Q. D. 2005, *ApJ*, 628, 205
- Tang S., Wang Q. D., Lu Y., Mo H. J., 2009, *MNRAS*, 392, 77
- Tang S., & Wang Q. D., 2009, *astroph/arXiv0902.0403*
- Takahashi H., Okada Y., Kokubun M., Makishima K., 2004, *ApJ*, 615, 242
- Wang Q. D. 2007, *EAS*, 24, 59
- White R. E., & Chevalier R. A. 1983, *ApJ*, 275, 69
- Wolfire M. G., McKee C. F., Hollenbach D., Tielens A. G. G. M., 1995, *ApJ*, 453, 673
- Zhao, H. S. 1994, Ph.D. thesis, Columbia Univ.

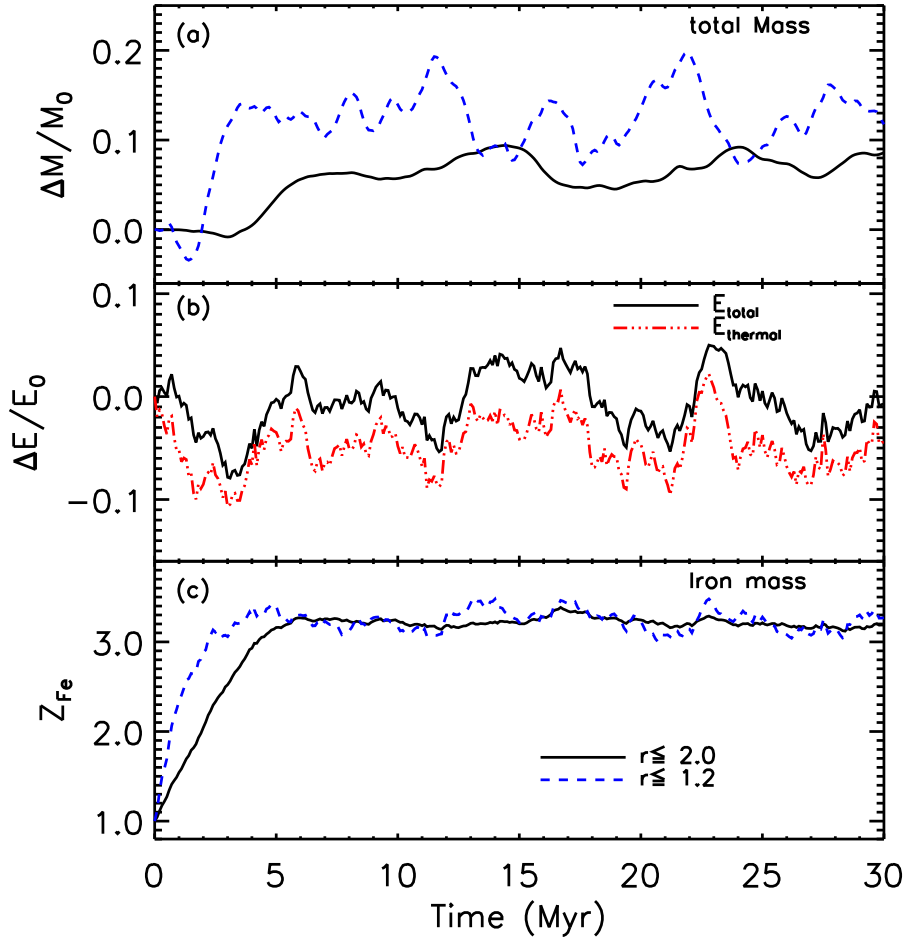


Fig. 1.— Variation of the total gas mass [panel (a)] and energy [panel (b)] relative to their initial values and iron abundance [panel (c)] in Model A. Dash blue lines show the variation within 1.2 kpc; other lines show the variation within 2.0 kpc. The three-dots-dash red line in panel (b) denotes the variation of the total thermal energy.

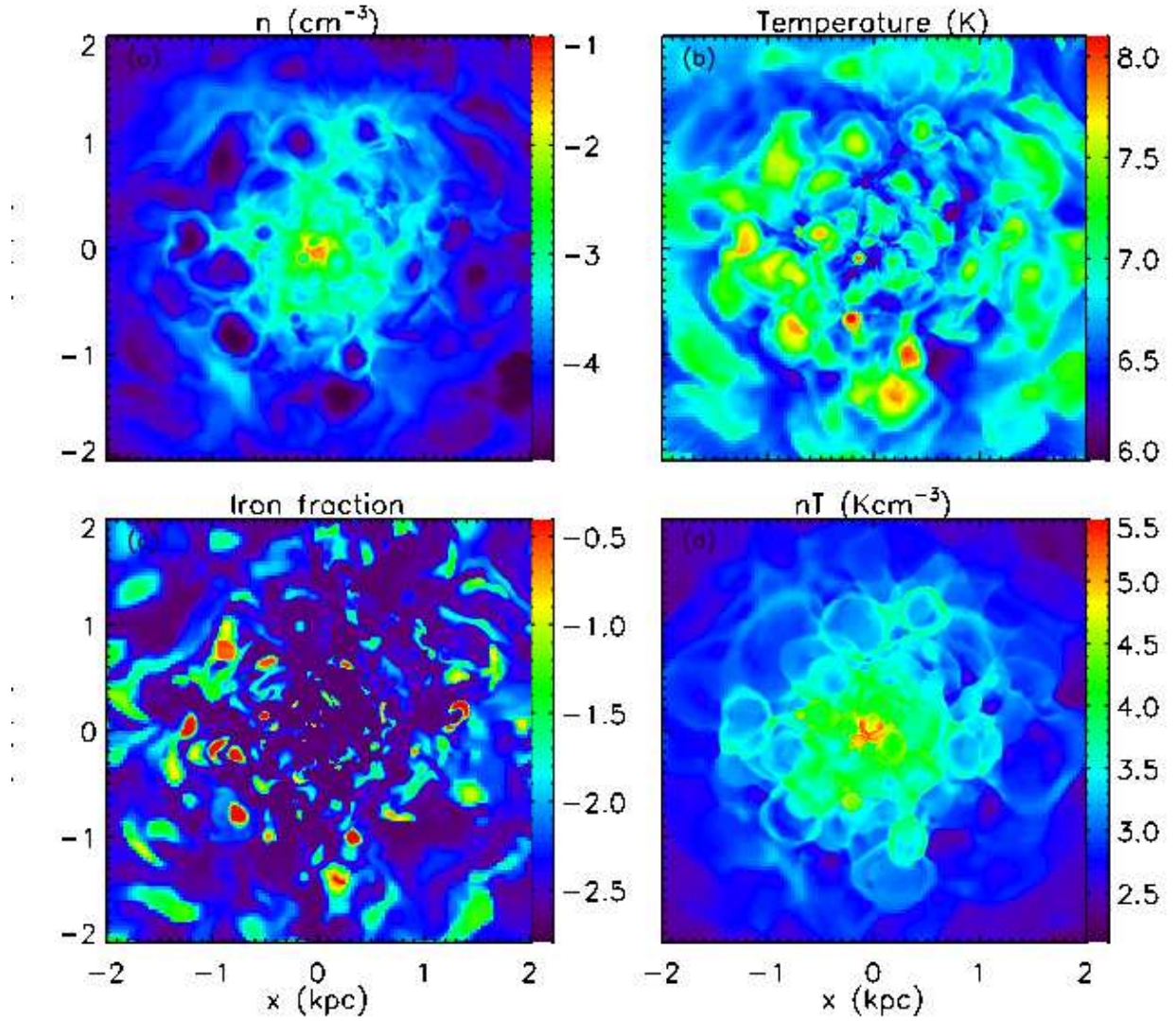


Fig. 2.— Snapshot of Model A in the $z = 2$ pc plane, showing (a) density, (b) temperature, (c) iron mass fraction, and (d) pressure. All plots are logarithmically scaled according to the color bars. Note that the upper right quarter region in each panel denotes the data from the octant at full resolution.

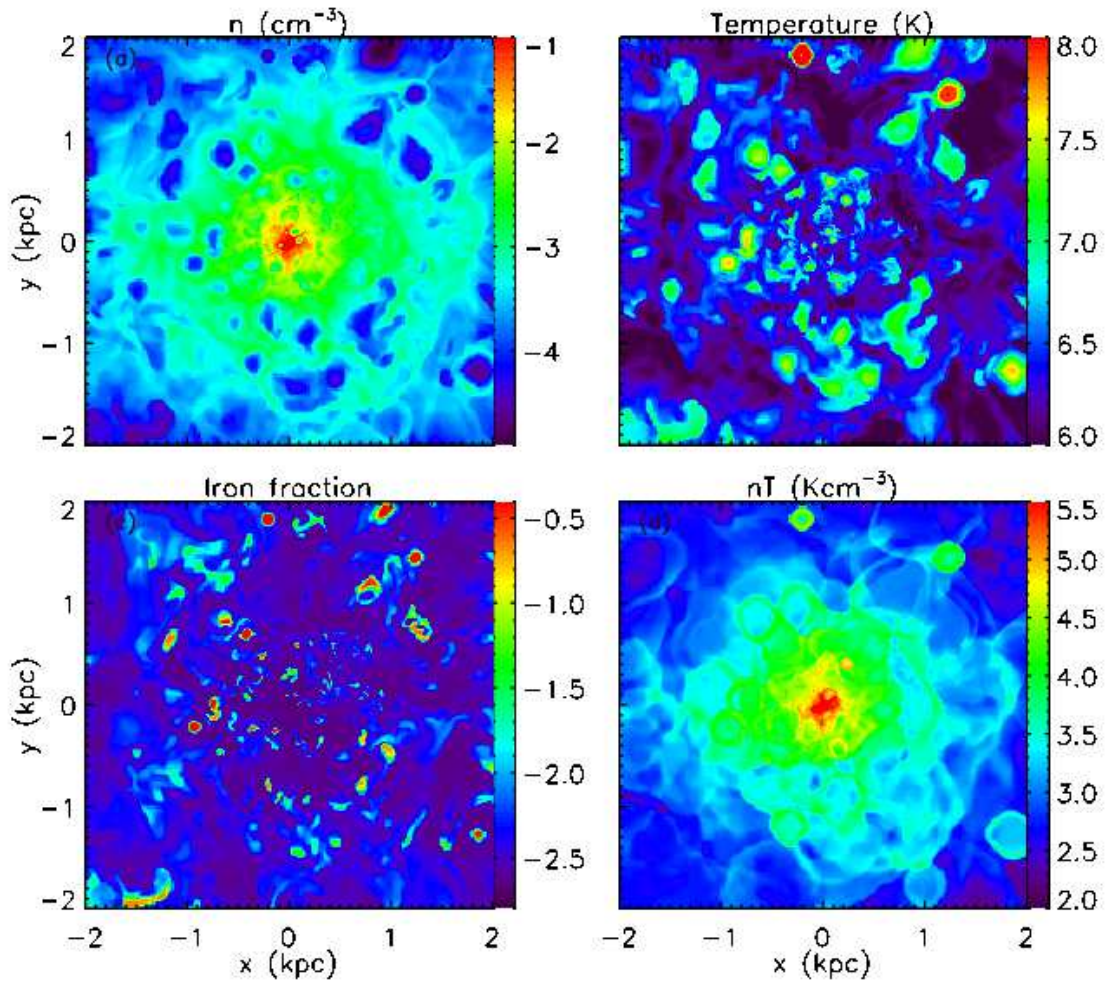


Fig. 3.— Snapshot of Model B in the $z = 2.5$ pc plane. All plots have the same meaning as in Fig. 2.

Table 2. Time-averaged X-ray Luminosities

Energy band(keV) (ergs s ⁻¹)	0.2-0.5 (10 ³⁶)	0.5-2.0 (10 ³⁶)	2.0-10 (10 ³⁶)	Iron K α (10 ³²)
(A) 1D: Z _⊙ /3.5 Z _⊙	0.092/0.22	0.72/2.42	0.022/0.066	0.095/0.31
(A) 3D: Z _⊙ /3.5 Z _⊙	0.39/1.18	1.22/4.14	0.021/0.062	4.1/13.8
(B) 1D: Z _⊙ /1.8 Z _⊙	3.44/5.32	10.8/18.5	0.03/0.05	... / ...
(B) 3D: Z _⊙ /1.8 Z _⊙	26.8/49.8	29.09/50.4	0.066/0.10	7.9/13.5

Note. — For each model the X-ray emissions are calculated using two metallicities: 1.0 and 3.5 solar for Model A; 1.0 and 1.8 solar for Model B.

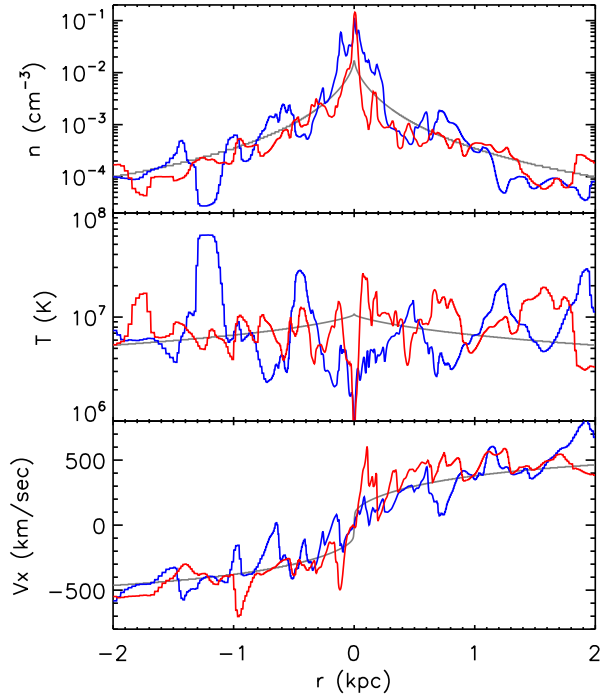


Fig. 4.— Two sample realizations of density, temperature, and velocity profiles along x -axis. The 1D results (gray lines) are included for comparison.

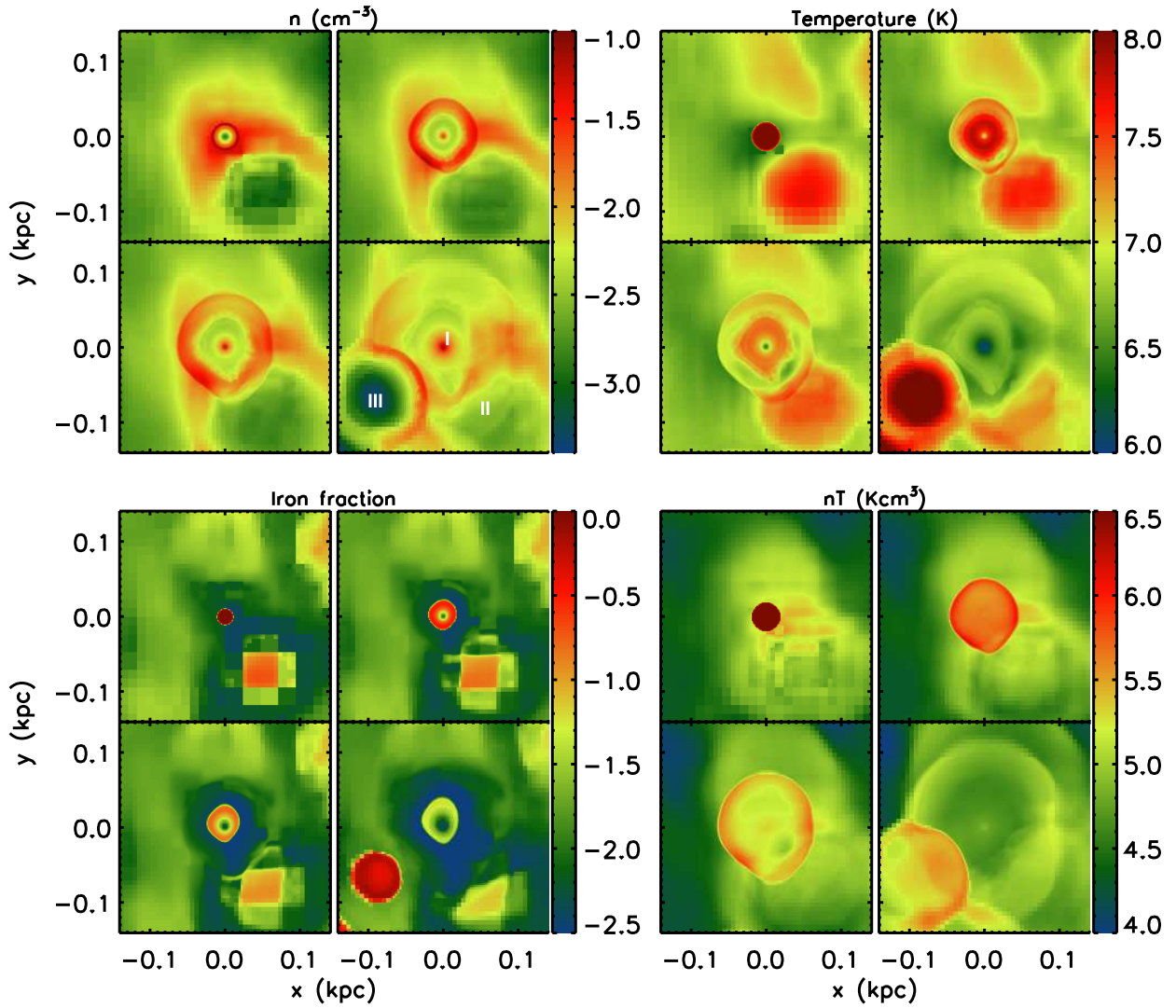


Fig. 5.— A sample SNR (centered at I) evolving near the bulge center. The density, temperature, iron fraction, and pressure are grouped into four large panels; each panel gives snapshots at four ages: 10^3 , 2.0×10^4 , 4.0×10^4 , 9.0×10^4 year, ordered from left to right and top to bottom. All values are logarithmically scaled according to the color bars.

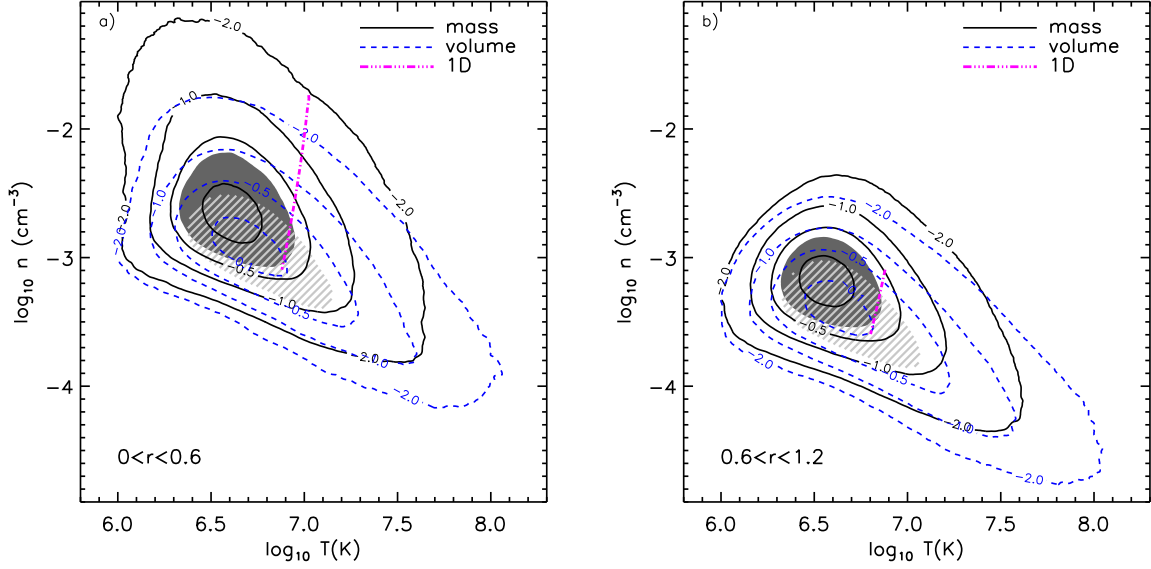


Fig. 6.— Gas mass (solid black) and volume (dash blue) distributions in the temperature-density space in two regions: $r \leq 0.6$ kpc (left panel) and $0.6 < r < 1.2$ kpc (right panel). Contours are normalized to their peak values and labelled logarithmically. The shaded regions denote the 50% coverage for the mass (solid shading region) and volume (hatched shading region) centered on their respectively peak values. The corresponding results of the 1D model are shown by the three-dots-dashed magenta line in each panel.

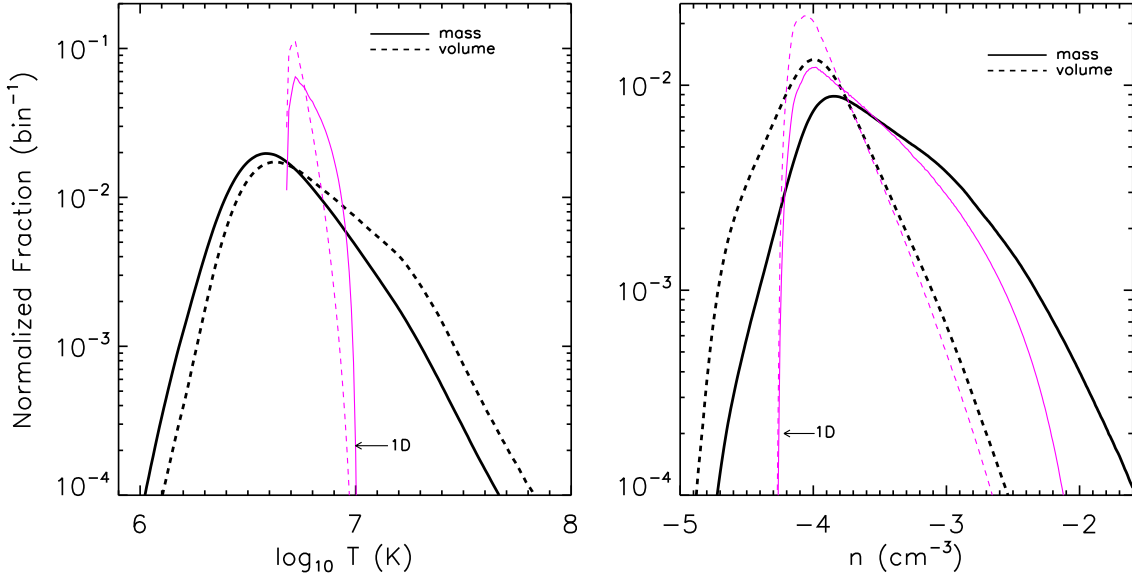


Fig. 7.— Gas mass (thick solid) and volume (thick dash) distributions as functions of temperature (left-panel) and density (right-panel) within $r < 1.2$ kpc. The corresponding distributions of the 1D model are shown in thin magenta lines.

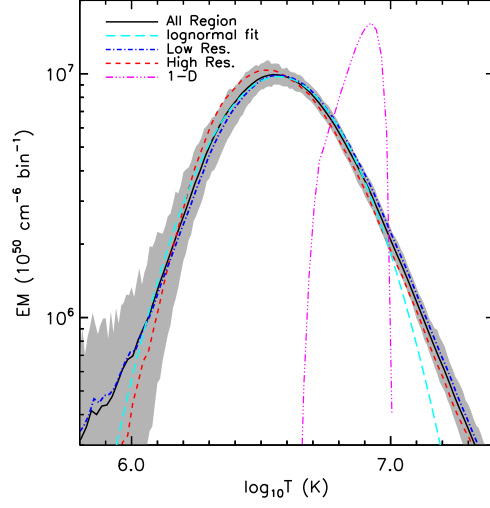


Fig. 8.— Time-averaged EMs as a function of temperature: the whole simulation region (solid black line); the low resolution octants (dash-dot blue line); the high resolution octant (short dash red line); and the 1D model (three-dots-dashed magenta line). The EMs of the low and high resolution regions are linearly scaled to the whole region according to their respective volumes. The grey region marks the 50% range around the mean EM of the whole region. Long-dash cyan line is a log-normal fitting with the mean $\log_{10} T = 6.57$ and the standard deviation of 0.24. The bin size of the temperature is 0.01 on the logarithmic scale.

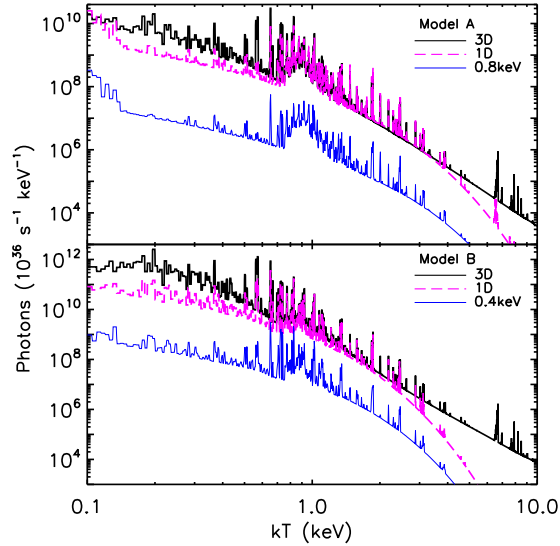


Fig. 9.— Time-averaged spectra within $r < 1.2$ kpc (solid black line) of Model A (top panel) and Model B (bottom panel), compared with their corresponding 1D model (dashed magenta line) and arbitrarily normalized spectra of isothermal plasma with a temperature of 0.8 keV or 0.4 keV. The solar abundance is used to generate all the spectra.

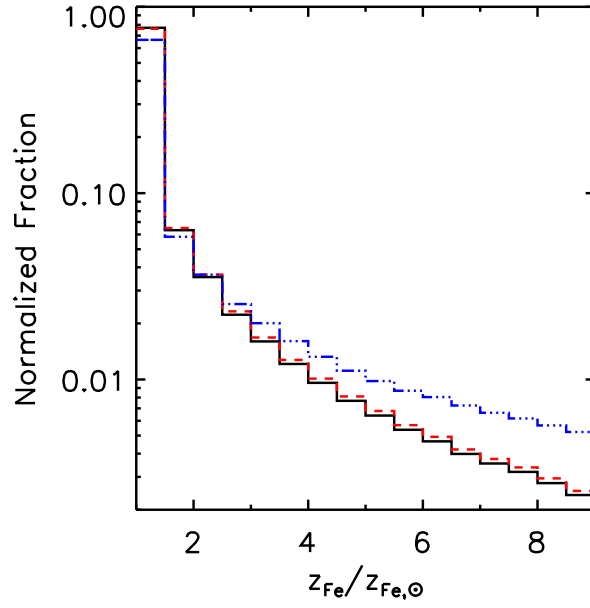


Fig. 10.— Distribution of the emission measure (solid line), as well as the luminosities in the 0.3-2.0 keV (dash red line) and the 2.0-5.0 keV (three-dots-dash blue line) bands as functions of the iron mass fraction.

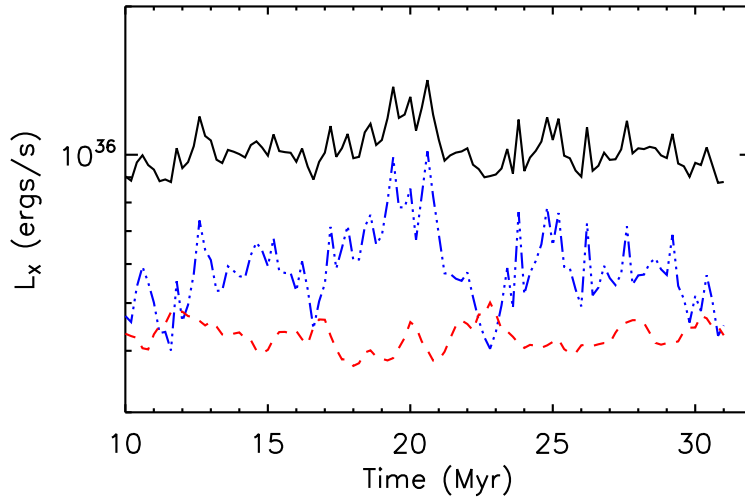


Fig. 11.— Illustration of the 0.3-2.0 keV luminosity fluctuation as a function of time in the region within $r \leq 0.6$ kpc (three-dots-dash blue line), between $0.6 \leq r \leq 1.2$ kpc (dash red line), and the total volume (solid black line).

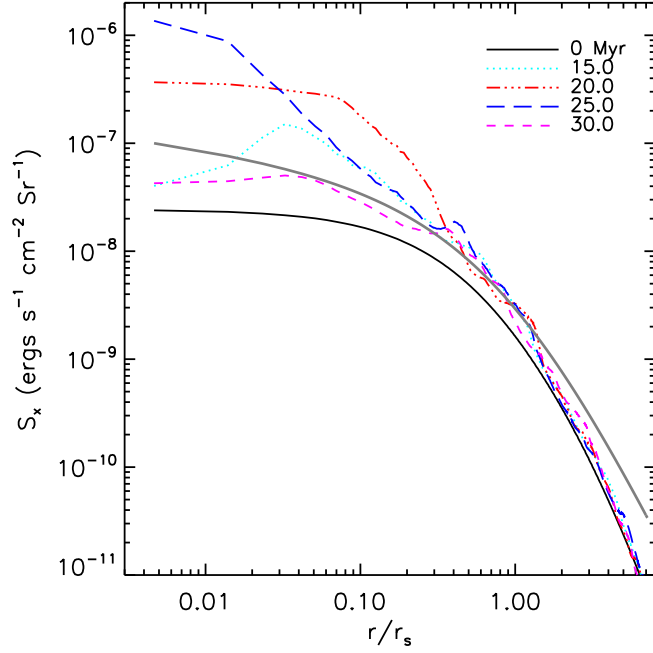


Fig. 12.— Sample projected radial intensity profiles in the 0.3–2.0 keV band. The gray line shows the assumed stellar surface density distribution with an arbitrary normalization.

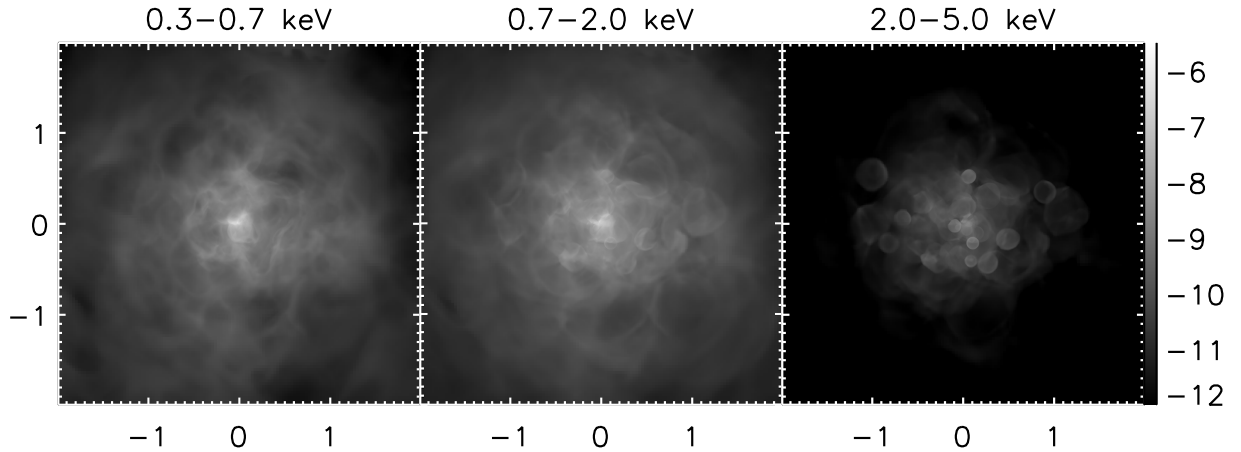


Fig. 13.— Representative intensity maps at full numerical resolution in the three energy bands. The unit of x and y axis is kpc. The intensity is in the units of $\text{ergs s}^{-1} \text{sr}^{-1}$ and is logarithmically scaled.

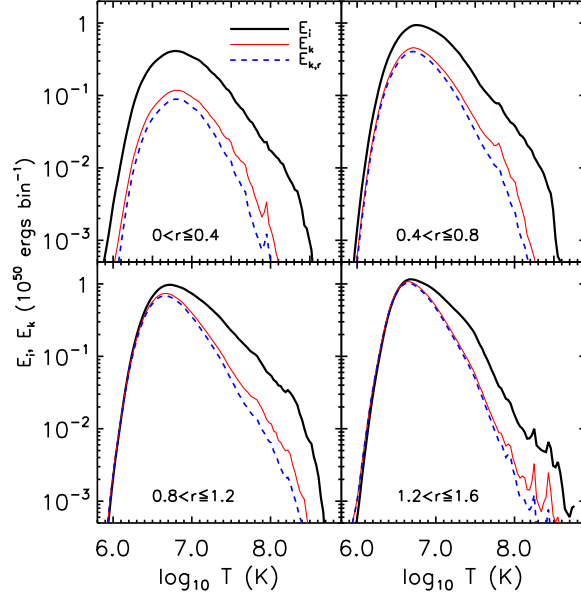


Fig. 14.— Time-averaged thermal (E_i) and kinetic energy (E_k ; $E_{k,r}$ is the radial component) distributions versus the gas temperature in four radial ranges as marked at the bottom of each panel.

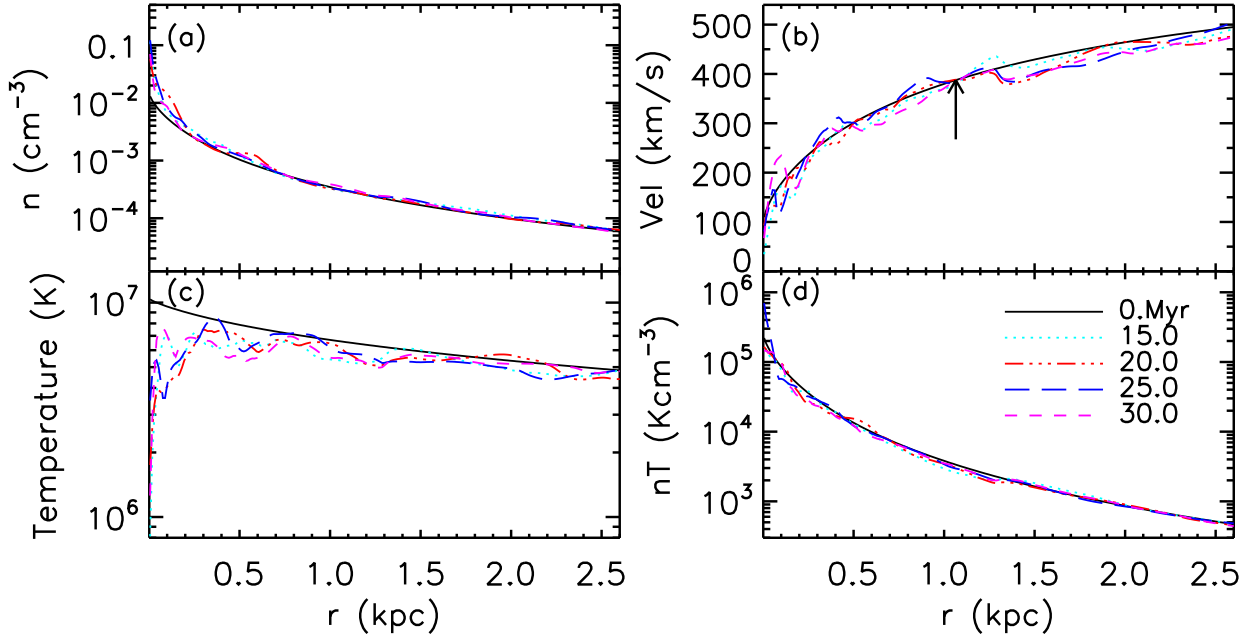


Fig. 15.— Radial profiles of density (a), velocity (b), temperature (c), and pressure (d) sampled at four times. The solid lines ($t=0.0$ Myr) show the 1D results. The density profile is weighted by volume and the other profiles are weighted by mass. The arrow in panel (b) marks the sonic point of the 1D model.

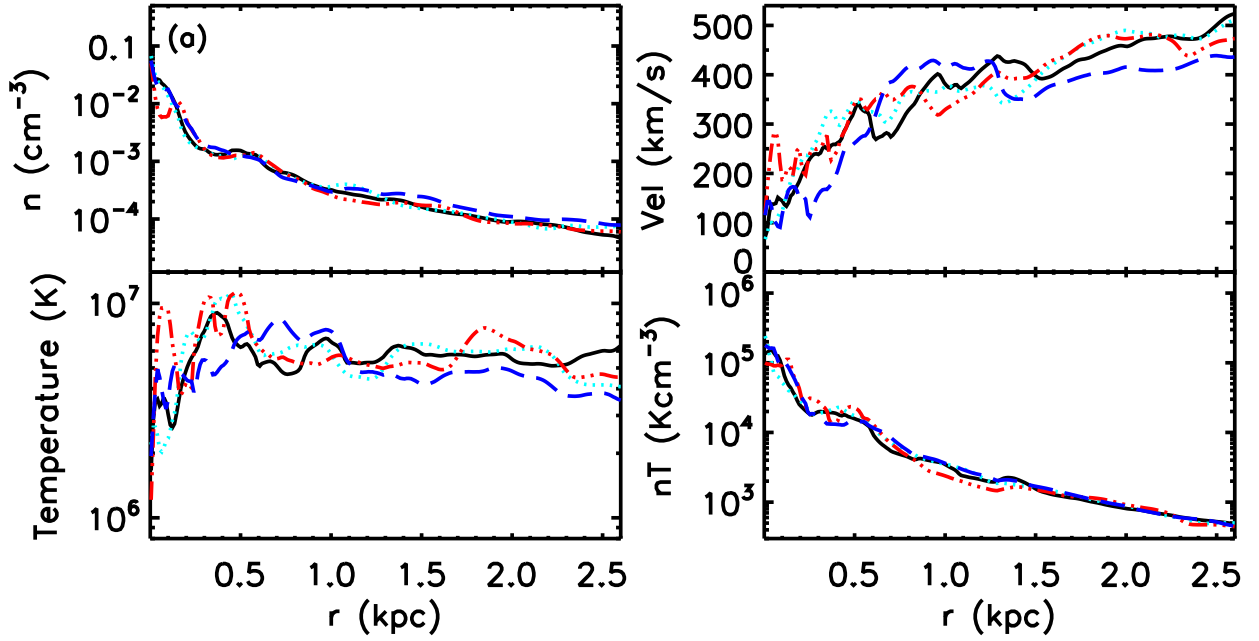


Fig. 16.— Radial profiles of density (a), velocity (b), temperature (c), and pressure (d) sampled at four octants. The solid black lines show the results of the octant at full resolution, and other lines of three octants of low resolution.

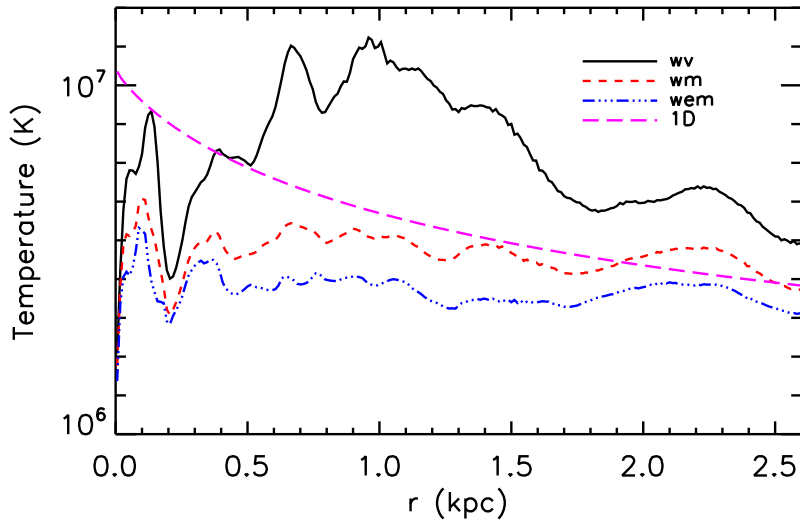


Fig. 17.— A sample radial temperature distribution weighted by volume (denoted as wv), by mass (wm), and by emission measure (wem). The long dash line denotes the 1D temperature profile.

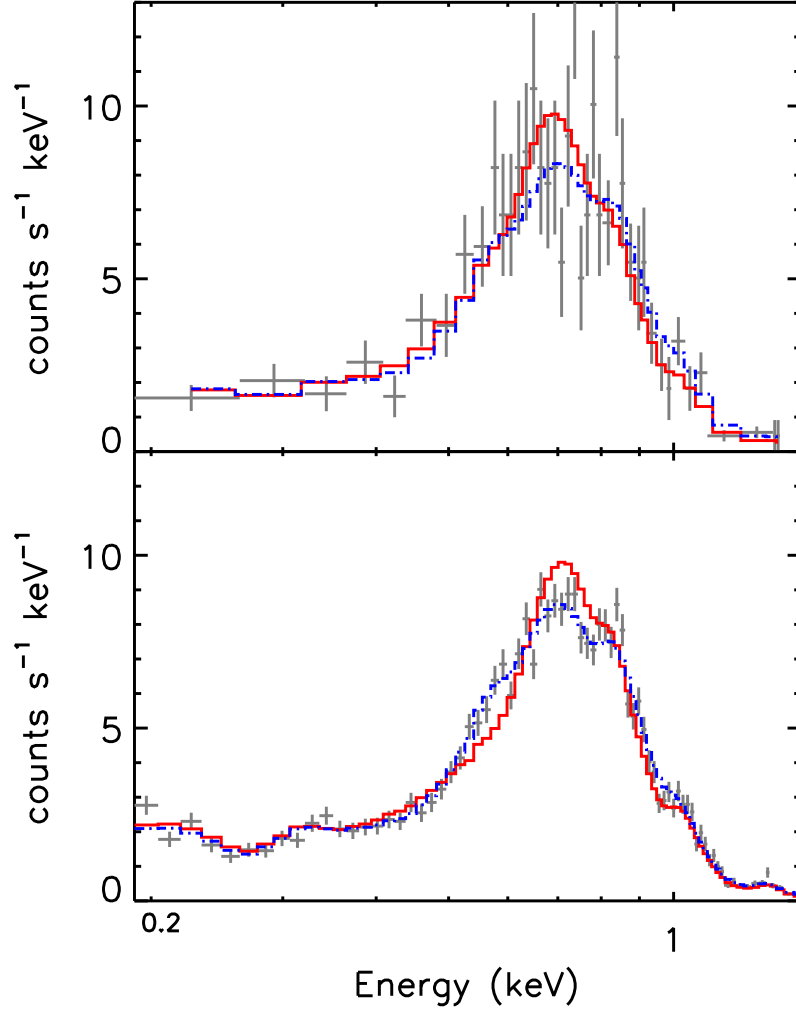


Fig. 18.— Simulated *Chandra* ACIS spectra of the X-ray emission from the modeled bulge gas, based on the differential EM shown in Fig. 8. About 600 and 10^4 photons are generated for the upper and lower panels, respectively. The solid red line denotes the fit of an isothermal plasma model while the dash-dot blue line denotes the simulated spectrum. The normalization is arbitrary.

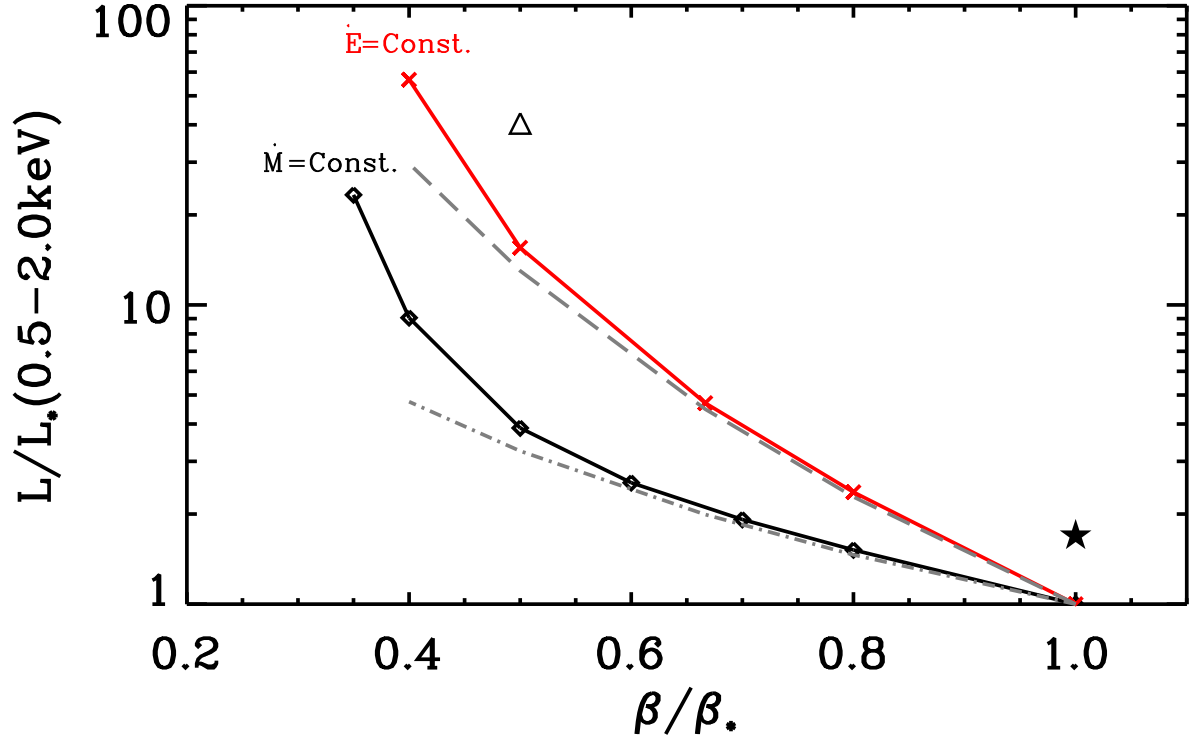


Fig. 19.— Dependence of the 0.5-2.0 keV luminosity on β . The linked diamonds denote the results with a fixed \dot{M} , while the crosses mark the results with a fixed \dot{E} . The 3D simulations results are marked by the star for Model A and the triangle for Model B. Gray lines denote the corresponding scaling relationship (see §4.3).

A. SNR Embedding Scheme

After all quantities of zones within the affected region are replaced by the dynamically generated SNR profiles, we make additional adjustments to conserve the mass, momentum, and energy, accounting for the geometrical effect due to discrete zones and the possible net bulk motion of gas in that region. Some symbols are introduced in the following adjustments for clarity: “M” denotes the total mass; “MX”, “MY” and “MZ” are momentum in X, Y and Z directions, respectively; “EK” is the total kinetic energy; “EI” is the total thermal energy; the subscripts “0” and “1” denote the values before and after the SNR seed is planted, “2” stands for the adjusted values. The symbols followed by (i, j, k) denote the values at each zone. In all the calculation a sub-zone method (e.g., subdividing a zone to determine whether a zone is partially within the affected region) is used in order to achieve high accuracy.

(a) Conservation of mass. It is accomplished by simply multiplying a factor, $f_{dens} = M_2/M_1 = (M_0 + M_{ejecta})/M_1$, to the density of scaled SN profile:

$$\rho_2(i, j, k) = f_{dens} \times \rho_1(i, j, k) . \quad (\text{A1})$$

$$M_0 = \sum_{i,j,k} \rho_0(i, j, k) \Delta V_{i,j,k} \quad (\text{A2})$$

$$M_1 = \sum_{i,j,k} \rho_1(i, j, k) \Delta V_{i,j,k} \quad (\text{A3})$$

M_{ejecta} denotes the SN Ia ejecta and is $1.4 M_\odot$. The summation ($\Sigma_{i,j,k}$) is over the SNR affected regions. Note that the change of mass will also affect the conservations of other values such as momentum and energy so this step must be done first. In general, f_{dens} is very close to one, which is guaranteed by the dynamically generated SNR profile.

(b) Conservation of momentum. There is no net momentum in each direction for the SNR seeds. However, the region to embed the SNR may contain non-zero momentum, especially when an SNR actually explodes in an outflowing wind region. Taking the momentum in the X direction as an example: the initial net momentum in X direction is

$$MX_0 = \sum_{i,j,k} \rho_0(i, j, k) v_{x,0}(i, j, k) \Delta V_{i,j,k} , \quad (\text{A4})$$

In order to conserve the momentum, we add a bulk motion

$$\bar{v}_{x,1} = \frac{MX_0}{M_2} \quad (\text{A5})$$

to the embedded SNR velocity profile

$$v_{x,1}(i, j, k) = v_{x,sn}(i, j, k) + \bar{v}_{x,1} . \quad (\text{A6})$$

$$\text{MX}_1 = \sum_{i,j,k} \rho_2(i, j, k) v_{x,1}(i, j, k) \Delta V_{i,j,k} , \quad (\text{A7})$$

Here $v_{x,sn}$ is the velocity profile of the SNR template. Let $f_{vx} = \text{MX}_0/\text{MX}_1$, thus

$$v_{x,2}(i, j, k) = f_{vx} \times v_{x,1}(i, j, k) . \quad (\text{A8})$$

The same procedure is also applied to Y and Z direction.

(c) Conservation of energy. The kinetic energy of the region is

$$EK_0 = \frac{1}{2} \sum_{i,j,k} \rho_0(i, j, k) \left(v_{x,0}^2(i, j, k) + v_{y,0}^2(i, j, k) + v_{z,0}^2(i, j, k) \right) \Delta V_{i,j,k} \quad (\text{A9})$$

After adjusting the mass and momentum, the updated kinetic energy is:

$$EK_2 = \frac{1}{2} \sum_{i,j,k} \rho_2(i, j, k) \left(v_{x,2}^2(i, j, k) + v_{y,2}^2(i, j, k) + v_{z,2}^2(i, j, k) \right) \Delta V_{i,j,k} . \quad (\text{A10})$$

The energy conservation is achieved by adjusting the thermal energy accordingly:

$$p_2(i, j, k) = f_{EI} p_1(i, j, k), \quad (\text{A11})$$

where

$$f_{EI} = \frac{EI_0 + EK_0 + E_{sn} - EK_2}{EI_1}, \quad EI_0 = \sum_{i,j,k} \frac{p_0(i, j, k)}{\gamma - 1} \Delta V_{i,j,k}, \quad EI_1 = \sum_{i,j,k} \frac{p_1(i, j, k)}{\gamma - 1} \Delta V_{i,j,k}. \quad (\text{A12})$$

Note the original random motion of mass inside the affected region is implicitly converted to thermal energy. The clumpy environment is also smoothed out by this scheme, and the embedded SNR is spherical symmetry related to the SNR center.